

University of Central Florida

**STARS**

---

Electronic Theses and Dissertations

---

2019

## Asteroid Surfaces: The Importance of Cohesive Forces

Keanna Jardine

*University of Central Florida*



Part of the [Astrophysics and Astronomy Commons](#), and the [Physics Commons](#)

Find similar works at: <https://stars.library.ucf.edu/etd>

University of Central Florida Libraries <http://library.ucf.edu>

This Masters Thesis (Open Access) is brought to you for free and open access by STARS. It has been accepted for inclusion in Electronic Theses and Dissertations by an authorized administrator of STARS. For more information, please contact [STARS@ucf.edu](mailto:STARS@ucf.edu).

---

### STARS Citation

Jardine, Keanna, "Asteroid Surfaces: The Importance of Cohesive Forces" (2019). *Electronic Theses and Dissertations*. 6607.

<https://stars.library.ucf.edu/etd/6607>

**ASTEROID SURFACES: THE IMPORTANCE  
OF COHESIVE FORCES**

by

KEANNA JARDINE

B.S. Adelphi University, 2016

A thesis submitted in partial fulfillment of the requirements  
for the degree of Master of Science  
in the Department of Physics  
in the College of Science  
at the University of Central Florida  
Orlando, Florida

Fall Term  
2018

Major Professor: Adrienne Dove

© 2018 Keanna Jardine

## ABSTRACT

Adhesive forces play a significant role on airless bodies due to their weak gravities. Investigating adhesion at the surface of asteroids and their constituent components is vital to understanding their formation and evolution. Previous research has been done to understand the interaction of micron-sized spheres to planar surfaces and sphere-to-sphere interactions, which have been used to develop models of asteroid surfaces. Our investigation experimentally investigates adhesion through atomic force microscopy (AFM) measurements between JSC-1 simulant particles and several AFM tips, including a typical pyramidal gold tip and microspheres of sizes 2  $\mu\text{m}$  and 15  $\mu\text{m}$ . The samples of JSC-1 consist of three size ranges: < 45  $\mu\text{m}$ , 75-125  $\mu\text{m}$ , and 125-250  $\mu\text{m}$ . For each sample we looked at the magnitude and distribution of the measured adhesive forces. Results show that the pyramidal tip produced larger forces than the spherical tips generally, and the sample that produced larger forces and a larger distribution of those force was the smaller, more powder-like sample with sizes <45  $\mu\text{m}$ .

## ACKNOWLEDGMENTS

I would like to thank all those involved in this project, without your dedication and faith in me and this project this would not be possible. First, I would like to thank God for guiding me and providing me with strength to accomplish this feat. I would also like to thank my thesis chair, and advisor Dr. Adrienne Dove. It was her guidance, calm but stern nature and excitement that brightened my dark days and helped me to reach this far. I would also like to thank my mentor and second committee member Dr. Laurene Tetard who guided me from the day I started graduate school and continues to let me know every chance allowed that I am going to accomplish great things. Thank you both for your time, patience, and ideas regarding this project and for being great mentors. I would also like to thank Dr. Dan Britt, my third committee member whose input and direction has helped keep me on track and for the constructive criticism.

I would also like to thank the University of Central Florida and Department of Physics for providing the opportunities to explore my research. It has allowed my scientific potential and knowledge to grow exponentially.

I would also like to extend a thank you all my amazing family, and friends for unwavering emotional and mental support over the years. I would also like to thank Mikhael Soliman who patiently took his time to teach and explain many of the instruments and analysis. Lastly, I would like to thank my Father who has been my rock throughout this process and graduate school. This one is for you.

## TABLE OF CONTENTS

LIST OF FIGURES.....	vii
LIST OF ACRONYMS (or) ABBREVIATIONS .....	x
CHAPTER 1: INTRODUCTION .....	1
1.1 Introduction.....	1
1.2 Asteroid Environment .....	5
1.3 Characterizing Asteroid grain size distributions .....	9
1.4 The Role of Adhesion on Asteroids .....	10
1.5 Requirement of Nanoscale Characterization.....	11
1.6 Atomic Force Microscopy.....	12
1.6.1 AFM Operating Principle.....	13
1.6.2 Theory .....	14
1.7 Previous Work.....	15
1.8 Thesis structure .....	15
CHAPTER 2: METHODS .....	16
2.1 JSC 1- Sample.....	16
2.2 AFM Operation .....	18
2.2.1 Force Curves .....	19
CHAPTER 3: RESULTS .....	21

3.1 Experimental Setup .....	21
3.2 Force Curves Measurements .....	22
3.2.1 Abnormal Curves .....	24
3.3 Calibration .....	26
3.4 Histograms .....	27
3.4.1 2 $\mu\text{m}$ Spherical Tip Histograms .....	29
3.4.2 15 $\mu\text{m}$ Histograms .....	31
3.5 Comparison of Histograms .....	32
CHAPTER 4: DISCUSSION .....	34
4.1 Interpretation of the Results .....	34
4.2 Future Work .....	37
REFERENCES .....	39

## LIST OF FIGURES

Figure 1 Top left: Asteroid (25143) Itokawa (~550m x 300m x 200m) displaying the rubble structure on the surface which consists of boulders, and fine grains. Top Right: Approach of the Hayabusa 2 spacecraft to Asteroid (162173) Ryugu (~1000m diameter) which also displays larger boulder like structures. Bottom: Asteroid (433) Eros (~17km mean diameter) displaying a less rubble like structure with a cratered surface. .... 2

Figure 2. Asteroid size vs. spin period with binaries and tumblers identified. All other bodies are single uniform rotators. As shown, no object larger than 1 km spins faster than ~2.4 h, which is known as the gravity spin barrier. This means that at those sizes, gravity dominates any strength effect. The smaller rapid rotators on the upper left of the graph experience tensile stress. Thus, it is inferred that they have cohesive strength holding them together. Credit: Scheeres *et al.*, 2015 6

Figure 3. Asteroid macroporosity estimated by subtracting the average porosity of asteroid’s meteorite analogue from the bulk porosity. Since micro porosity probably does not seriously affect the structural integrity of asteroids, this is a direct estimate of the large-scale fractures and voids that determine the asteroid’s internal structure. Credit: Britt *et al.*, 2002..... 7

Figure 4. Schematic of AFM setup ..... 13

Figure 5. Bulk Elemental composition of JSC-1 simulant as compared to Lunar soil. Credit: McKay *et al*, 1994..... 17

Figure 6. Cross-section of a typical JSC-1 simulant grain consisting of Glass (GL), Olivine (OL), and Plagioclase (PL). Credit: McKay *et al*, 1994 ..... 18

Figure 7. Example force curve showing the approach to the sample (A), the snap in of the tip to the sample (B), the local deformation of the sample (C), the initial retracting of the tip from the sample (D), and the complete removal of the tip from the sample (E)..... 20

Figure 8. Picture of the characteristics of the two tips used in the experiment (right) and a table of their key characteristics, which may influence the measurements (left). ..... 22

Figure 9. A force-separation curve of the pyramid shaped tip on the less than 45  $\mu\text{m}$  sample, showing the deflection in volts (V) and the displacement in nm..... 23

Figure 10. A force-separation curve of the 2  $\mu\text{m}$  sphere on the less than 45  $\mu\text{m}$  sample.

Oscillations in the approach and retract curves are attributed to the limitations of the system....	23
Figure 11. the force displacement curve of the 15 $\mu\text{m}$ sphere on the 125-250 $\mu\text{m}$ sample.	
Oscillations in the approach and retract curves are attributed to the machine and the cantilever	24
Figure 12. An example of abnormal force curve obtained on the 75-125 $\mu\text{m}$ sample using the pyramid gold tip.....	25
Figure 13. An example of abnormal force curve obtained with the 2 $\mu\text{m}$ sphere, on the 75-125 $\mu\text{m}$ sample.....	25
Figure 14. An example of abnormal curve obtained from the 15 $\mu\text{m}$ sphere tip on the < 45 $\mu\text{m}$ sample. ....	26
Figure 15. Histogram displaying the distribution of measured adhesion force values between 3 grains on the 75-125 $\mu\text{m}$ sample and the pyramid-shaped tip. ....	28
Figure 16 Histogram displaying the distribution of measured adhesion force values between 2 grains on the 125-250 $\mu\text{m}$ sample and the pyramid-shaped tip. ....	28
Figure 17 Histogram displaying the distribution of measured adhesion force values between 3 grains on the < 45 $\mu\text{m}$ sample and the 2 $\mu\text{m}$ spherical tip. ....	29
Figure 18. Histogram displaying the distribution of measured adhesion force values between 3 grains on the 75-125 $\mu\text{m}$ sample and the 2 $\mu\text{m}$ spherical tip.....	30
Figure 19 Histogram displaying the distribution of measured adhesion force values between 3 grains on the 125-250 $\mu\text{m}$ sample and the 2 $\mu\text{m}$ spherical tip. ....	30
Figure 20. Histogram displaying the distribution of measured adhesion force values between 3 grains on the < 45 $\mu\text{m}$ sample and the 15 $\mu\text{m}$ spherical tip.....	31
Figure 21. Histogram displaying the distribution of measured adhesion force values between 2 grains on the 75-125 $\mu\text{m}$ sample and the 15 $\mu\text{m}$ spherical tip.....	31
Figure 22. Histogram displaying the distribution of measured adhesion force values between 3 grains on the 125-250 $\mu\text{m}$ sample and the 15 $\mu\text{m}$ spherical tip. ....	32
Figure 23. Pyramid-shaped tip vs. 2 $\mu\text{m}$ spherical tip vs 15 $\mu\text{m}$ spherical tip. Comparison of histograms across all samples and tip types.....	33
Figure 24. SEM images of the < 45 $\mu\text{m}$ sample (left) and the 75-125 $\mu\text{m}$ sample (right). A scale is shown in the bottom left of the picture for size comparisons. ....	35

Figure 25 Top: SEM image of the 75-125  $\mu\text{m}$  sample magnified to 250 X displaying smaller particles on the surface of a rock. Bottom: SEM image of the 75- 125  $\mu\text{m}$  sample magnified to 500 X displaying the smaller particles littering the surface of a rock. .... 36

Figure 26. Generic force curve showing the properties of the material and cantilever you can extract from a force curve. The circled properties are priorities for future analysis. .... 38

## LIST OF ACRONYMS (or) ABBREVIATIONS

AFM	Atomic Force Microscopy
cm	Centimeter
mm	Millimeter
nm	Nanometer
nN	Nanonewton
MB	Main Belt Asteroid
NEA	Near Earth Asteroid
SEM	Scanning Electron Microscope
SiO <sub>2</sub>	Silicon Dioxide
SPM	Scanning Probe Microscope
μm	Micrometer
V	Volts
XRD	X-ray Diffraction

# CHAPTER 1: INTRODUCTION

## 1.1 Introduction

Research on Near Earth Asteroids (NEAs) and main belt (MB) asteroid populations has evolved over the years to not only understanding their orbits, spin, class, and density, but to also understanding the mechanical properties of active and inactive asteroids that are determined by interaction with their environment and the forces that act on them. Although the database for NEAs continues to expand, many asteroids are very small and are often difficult to observe, especially to examine their surface features. Chapman (1978) coined the term “rubble pile” to represent solar system bodies with a diameter between 200 m and 10 km that are bound together by their own self gravity. Rubble piles are defined in Richardson *et al* (2002) as bodies that have nearly zero tensile strength and significant bulk porosity between the particles. Most of the scientific data used to characterize asteroids comes from the study of NEAs because of their close encounters with Earth, which allows ground-based observations of these bodies using radio telescopes, radar, and Doppler measurements to determine the rotation rates, shape, and some surface properties (Walsh, 2018). To date, only a few missions have been able to capture high-quality, multi-pixel images of the surfaces of asteroids such as Eros and Itokawa. These help to further define the upper limits to rubble pile diameters based on the images of both surfaces (Figure 1). Current sample return missions to two primitive asteroids are underway, OSIRIS-Rex (to Bennu) and Hayabusa-2 (to Ryugu).

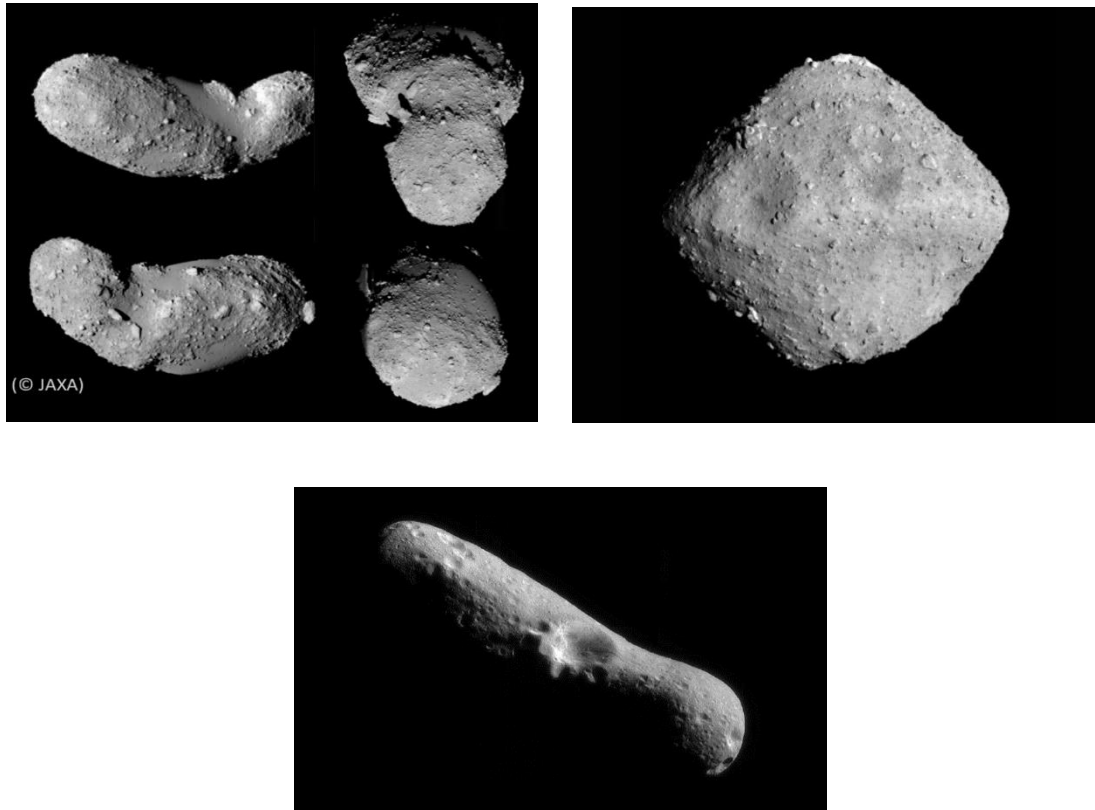


Figure 1 Top left: Asteroid (25143) Itokawa (~550m x 300m x 200m) displaying the rubble structure on the surface which consists of boulders, and fine grains. Top Right: Approach of the Hayabusa 2 spacecraft to Asteroid (162173) Ryugu (~1000m diameter) which also displays larger boulder like structures. Bottom: Asteroid (433) Eros (~17km mean diameter) displaying a less rubble like structure with a cratered surface.

Collisional processes have dominated the evolution of solar system bodies, and theories have developed through time to explain these observations. Roche (1847) first discussed a disruption limit of fluid, or strengthless, bodies when they make close encounters with planets. Jeffreys (1947) expanded this concept to solid bodies in an attempt to explain that Saturn's rings were not formed from the breakup of a large icy body orbiting closely to Saturn, leading to the conclusion that solid bodies were not likely to tidally disrupt close to a planet. This was refuted in 1965 after observations of a close encounter and breakup of the comet Ikeya-Seki with the Sun (Opik, 1966), which further expanded the conversation about strengthless bodies

bounded by self-gravity in our solar system. As technology has advanced and our knowledge of the MB has expanded, the largely collisional history of the asteroid belt has been revealed. Collisional evolution of large asteroids on the order of 100s of meters through catastrophic disruption is the likely source of the smaller asteroids we see today (Bottke *et al.*, 2005).

Catastrophic disruption of asteroids and the dispersal of their pieces are important to learning about their histories, but the accumulation of their pieces is important to finding out how rubble piles form. Shattering of asteroids plays an important role in larger asteroids, where the energy per mass required to shatter an object decreases as the size of the object increases (Holsapple, 1994; Walsh, 2018). Asphaug, *et al.* (2002) estimated a diameter of about 300 m as the crossover between strength- and gravity-dominated regimes for unfractured basalts. Collisions of smaller objects, where the largest piece is about 50% of the original mass, requires less dispersion energy because at small scales the strength of the body determines collisional results (Walsh, 2018). This is speculated to have happened on Mathilde, a rubble pile asteroid with large craters that would be expected to be due to an impact that would have broken the body apart, but it remains intact.

The cores of rubble pile asteroids are not fully understood, but imagery from Hayabusa suggests that they are made up of boulders that are on the order of tens of meters and less (Scheeres *et al.*, 2010). On the contrary, the spin rate statistics suggest that some objects of 100 m or less can spin at much faster rates, which suggests that instead of self-gravitating boulders, these objects must be solid bodies (Scheeres *et al.*, 2010).

The predictions made above are based on scaling the physics of Earth's environment

to the physics of the asteroid environment. However, these scaling relations are not fully understood, and it is difficult to perform experiments in a simulated asteroid environment that includes very low gravity. It is important to note that asteroids are prone to many different physical effects that shape their surfaces and sub-surfaces. These effects include electrostatic forces, friction, rotational forces, gravitational forces, and solar radiation pressure (Scheeres *et al.*, 2010).

Characterizing the adhesive values of asteroid materials is essential in asteroid and other small body research because adhesion plays a key role in asteroid structures, their evolution, and in surface features. By understanding surface properties such as adhesion and cohesion, we can examine the processes that form asteroids, develop models that predict their evolution and history, and better model their current behavior. Adhesion is described as the bond between two unlike materials/molecules and the force required to separate them and Cohesion is described as the mutual attraction of like substances and molecules which cause them to stick/bond.

Sample return missions would provide vital information on adhesive forces on asteroid surfaces but must be first informed by laboratory studies. Asteroid missions involve landing on and interacting with unknown materials in a low-gravity environment, which stresses the importance of knowing the properties of the interacting material. Additionally, the potential of a NEA impacting Earth is grounds for understanding in detail the adhesive properties of these airless bodies so that proper mitigation strategies can be implemented.

## 1.2 Asteroid Environment

Over the past few years, the size and spin distributions of asteroids have been compiled to show that there is a clear relationship between asteroid size and spin rate. This has been used as evidence that most asteroids are made of aggregates that are weakly bounded by cohesion forces (Scheeres *et al.*, 2010). The implications for larger asteroids suggest that they are made up of distinct bodies lying on each other and when they spin up, they break apart into their components that can either orbit each other, creating a binary asteroid system, or eventually escape each other. These separate bodies would continue to spin rapidly, eventually breaking down into smaller pieces that spin at high rates (Scheeres *et al.*, 2010). The smaller pieces of the escaped body are speculated to be the population of small rapid rotators as shown in Figure 2 (Sanchez and Scheeres, 2014).

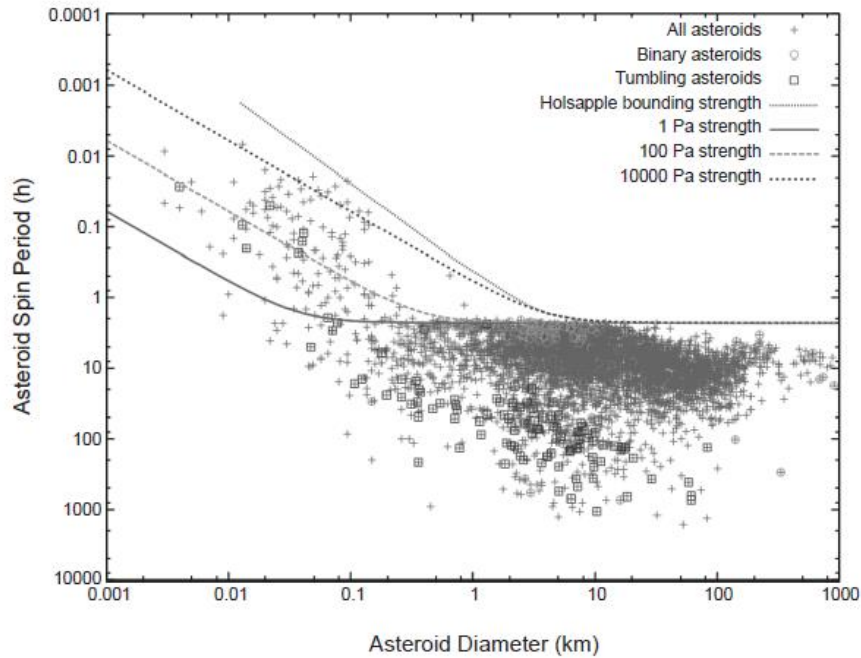


Figure 2. Asteroid size vs. spin period with binaries and tumblers identified. All other bodies are single uniform rotators. As shown, no object larger than 1 km spins faster than  $\sim 2.4$  h, which is known as the gravity spin barrier. This means that at those sizes, gravity dominates any strength effect. The smaller rapid rotators on the upper left of the graph experience tensile stress. Thus, it is inferred that they have cohesive strength holding them together.

Credit: Scheeres *et al.*, 2015

Additional evidence of differences in these rotators comes from measurements of their porosities. Data collected over the years has shown that asteroids have high bulk porosities. Figure 3 highlights the estimated bulk porosities of a few asteroids and it can be seen that low porosity asteroids are rare. Aside from the three largest asteroids, 1 Ceres, 4 Vesta, and 2 Pallas, the only observed asteroid with a porosity lower than 15% is 20 Massalia.

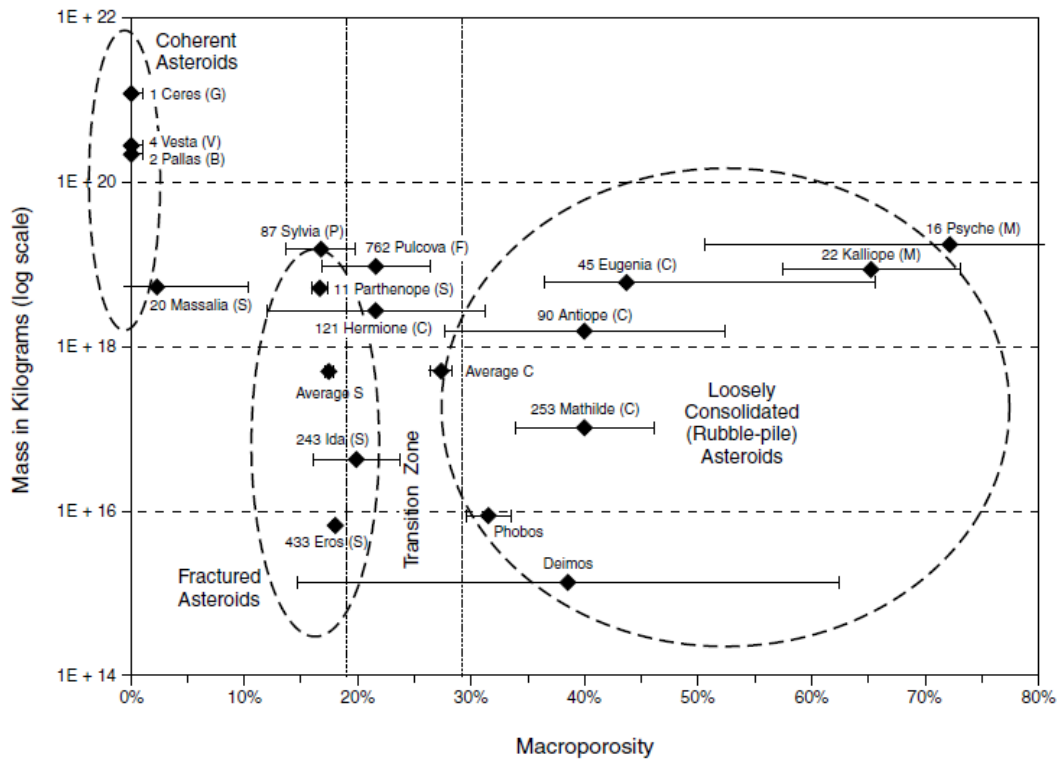


Figure 3. Asteroid macroporosity estimated by subtracting the average porosity of asteroid’s meteorite analogue from the bulk porosity. Since micro porosity probably does not seriously affect the structural integrity of asteroids, this is a direct estimate of the large-scale fractures and voids that determine the asteroid’s internal structure. Credit: Britt *et al.*, 2002

The porosities measured consider the micro porosities in meteorites and the large-scale macro porosity of the asteroid. The data separates into three groups. The first includes the largest asteroids which are intact bodies whose grain densities of their meteorites match their bulk density indicating almost no macroporosity. The second group includes asteroids that have between 15%-25% macroporosity indicating fracturing of the body, which was confirmed from spacecraft images of 433 Eros and 243 Ida, which are included in this group (Veveřka *et al.*, 2000). The fracturing on these bodies was not sufficient to cause a breakup of the object, which indicates some coherent strength in the body. Asteroids with less than

25% macroporosity most likely have some measure of coherent strength, and objects with porosities over 30% are most likely rubble piles (Britt *et al.*, 2002). Hence, the third group is most representative of rubble piles, with porosities ranging from 30% to more than 70%. This indicates more void space than in solid material. These asteroids were catastrophically disrupted and reaccumulated by self-gravity. Observations of binary asteroids allow for an estimation of the total mass, total volume, and density (Britt *et al.*, 2002). Porosity values are related to the type of asteroid with S-type asteroids starting at about 30% and C-type asteroids at about 50% (Scheeres *et al.*, 2010). Samples of meteorites were measured and were found to be 10% porous, which suggests that the higher parent body porosity must be from the overall structure (Scheeres *et al.*, 2010).

High-resolution images of Itokawa and Eros and the sample return from Itokawa provided details about objects on the small scale on both bodies. Eros showed fine materials smaller than the centimeter scale, and Itokawa showed boulders and fines on the millimeter to centimeter scale with the finest material at smooth, low-gravity areas on the body (which are often referred to as “ponds”) (Dombard *et al.*, 2010). This evidence suggests some movement of the grains across the surface.

Eros is one of the larger NEA’s with a porosity ranging from 21-33% and it has a homogenous gravity field and a uniform density (Dombard *et al.*, 2010). On the surface of Eros, much like Itokawa, there are “ponds” of fine regolith compared to its surroundings. Eros has a smooth, flat surface littered with large boulders and about 300 pond-like features (Dombard *et al.*, 2010). The ponds are formed in low-slope, high-elevation areas, which makes the regolith less mobile. The pond-like features have many possible mechanisms of

formation, including seismic shaking, electrostatic transport, mechanical erosion, micrometeorite spallation, and thermal weathering.

Itokawa's surface and subsurface have been observed to be dominated by boulders on the order of tens of meters and grains on the millimeter to centimeter scales (Fujiwara *et al.*, 2006). It has a bulk porosity of 40%. Itokawa is an S-type asteroid mostly composed of silicates and is suspected to be a rounded rubble pile body made of boulders (Fujiwara *et al.*, 2006). In fact, it shows evidence of a bimodal distribution, which suggests it is a binary object with two structures in contact (Scheeres *et al.*, 2010). The existence of boulders and pillars suggests an early collisional breakup from a larger asteroid and then a re-agglomeration. The smooth areas on the surface of the asteroid (Muses Sea and Sagami-hara) compared to the low gravity areas suggest mass movement. The accumulation of the small grains on Itokawa is thought to be caused by seismic shaking from impacts, shifting tidal loads, and the movement of grains through the voids within the asteroid (Fujiwara *et al.*, 2006).

### 1.3 Characterizing Asteroid grain size distributions

Regolith grain size can be used to estimate the cohesive strength of the regolith (Gundlach and Blum, 2013). Grain sizes can be determined through models and remote observations, fly-by missions, and sample return missions. While high-resolution images are lacking for most asteroids, other measurements can be used to determine grain sizes and distributions. The porosity and the size of the particles determine how the surface responds to solar irradiation, and this can be observed with measurements that indicate the body's thermal

inertia responses (Housen and Holsapple, 2011; Guttler *et al.*, 2012; Kiuchi and Nakamura, 2014). In short, the thermal inertia of asteroids is an indication of whether the surface is covered with rocks and boulders or with fine powder-like regolith much like the lunar soil, whose porosity (51%) is used for comparison (Sanchez & Scheeres., 2014). Generally, thermal inertia measurements suggest that small bodies are covered by coarse grains in the mm to cm scale, while the larger bodies are covered with finer grains, as seen on Eros. This can partially be explained by the fact that gravity on a larger body is larger, resulting in a higher escape velocity so the finer grains can be retained on the surface. Finer particles are also more adhesive than coarser particles and can act as a glue to hold the larger, coarser particles to the surface (Sanchez & Scheeres., 2014).

#### 1.4 The Role of Adhesion on Asteroids

There is some uncertainty in the structure of the cores of asteroids and how they compare to the more directly observable surface regolith. Although uncertain, seismic shaking is a widely discussed process that creates a “Brazil Nut” effect, where through vibrations or oscillatory movements the larger particles travel to the top layer and the smaller particles settle underneath. This effect was simulated numerically for Itokawa and Eros and was proven to be a viable explanation for the boulders and particle size distributions on the surfaces of these objects (Matsumura *et al.*, 2014).

Electrostatic levitation and transport constitute another mechanism that is suggested to depend on cohesive properties but has not been thoroughly investigated. The cohesive force

between small dust particles is important when considering the electrostatic force required to loft a particle off the surface because the cohesive forces dominate on airless bodies over the gravitational force (Hartzell *et al.*, 2012). Grain size is an important factor, and based on experiments and simulations, Hartzell *et al.* (2012) concluded that medium sized grains about 15  $\mu\text{m}$  in diameter required less force to loft than smaller ( $\sim 5\mu\text{m}$ ) and larger ( $\sim 25\mu\text{m}$ ) particles (Hartzell *et al.*, 2012).

### 1.5 Requirement of Nanoscale Characterization

Representing asteroid surfaces using realistic simulants and measuring the interacting forces can help us to extract meaningful values of the adhesion forces of realistic materials and a better understanding the forces between particles at small scales. For this, we can use Atomic Force Microscope (AFM) techniques to extract adhesive force values of simulant grains of different sizes and materials. We can expand this by using different particle sizes and AFM tip shapes (see details in Section 3.1). At this level, we can investigate the interactions of micron scale particles with each other which will inform models of adhesion in asteroid regolith on rubble piles. This investigation allows us to experimentally explore this interaction and draw conclusions based on how what happens at the nanoscale contributes to the bigger picture of characterizing rubble pile asteroids and understanding the mechanisms that hold them together and modify their structures.

## 1.6 Atomic Force Microscopy

In the early 1980s, a breakthrough with the development of the Scanning Probe Microscope (SPM) took the nanostructure analysis of materials to another level (Gomes *et al.*, 2001; Tararam *et al.*, 2017). SPM generates 3D images of the surface (Jalili and Laxminarayana, 2004; Tararam *et al.*, 2017) with nanoscale spatial resolution, and can be used either in air, vacuum, or liquid environment. SPM techniques generally use a sensing micro machined probe that interacts with the surface, feedback loops that control the position of the probe, a piezoelectric to position and scan the sample with respect to the probe, and a computer to store, process and analyze the data (Stadelmann, 2016; Tararam *et al.*, 2017).

Scanning Tunneling Microscopy (STM), in 1981, was the first SPM technique that was able to image the surface of a sample in atomic resolution and good conductivity (Tararam *et al.*, 2017). Atomic Force Microscopy (AFM), developed in 1986, modified a STM by replacing the conductive tip by a micro-cantilever, used to measure the sample surface morphology. The deflection of the cantilever is monitored with a read-out laser system, similar to a profilometer. This enables the measurement of tip-sample interactions for a wide range of materials (Binnig *et al.*, 1986; Tararam *et al.*, 2017). AFM contributed to the development of many other SPM techniques for functional measurements allowing a rapid development in the characterization of materials such as chemical interactions between samples and probes, mechanical properties like hardness, friction, and adhesion, as well as magnetic, thermal, and electrical properties.

### 1.6.1 AFM Operating Principle

The AFM uses a microcantilever with a sharp tip as a probe. The read-out system includes a laser aligned at the back end of the cantilever and reflected to a photodiode detector. The controller is used to control the tip-sample interaction and the image acquisition. The AFM measures the force between the tip and the sample through the deflection of the cantilever to track the topography of the sample. The deflection is measured using a laser diode that reflects off the top of the cantilever to the photodiode. If the deflection changes the photodiode detector signal changes, which is then recorded and sent to the controller, to adjust the interaction through a feedback loop. The controller then adjusts the vertical position of the cantilever with respect to the sample. The detector signal, in Volts, is converted into height images. The characteristics of the cantilever are a determining factor of the quality of the images because its spring constant and the shape of its tip influence the contact and interaction with the sample surface (Giessibl, 2003; Tararam *et al.*, 2017). A schematic of an AFM setup is displayed in Figure 4.

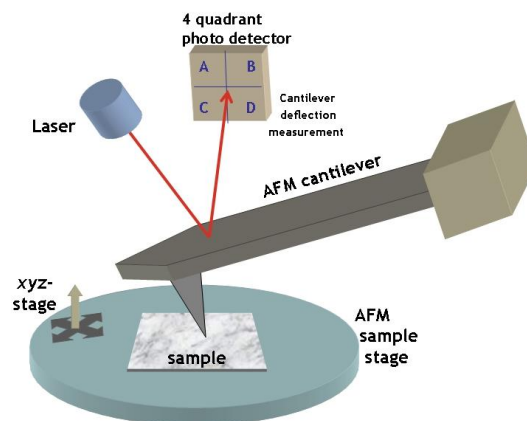


Figure 4. Schematic of AFM setup

### 1.6.2 Theory

The AFM tip and the sample interaction can be described using Hooke's Law, where the force ( $F$ ) is calculated from the product of the spring constant of the cantilever ( $k$ ) and the change in the deflection of the cantilever ( $\Delta x$ )

$$F = -k \cdot \Delta x \quad (1)$$

The relationship between the spring constant and the cantilever dimensions is defined by the equation:

$$k = \frac{Ewt^3}{4L^3}, \quad (2)$$

where  $w$  = cantilever width,  $t$  = cantilever thickness,  $L$  = cantilever length, and  $E$  = Young's modulus of cantilever material. Hooke's law can also be used to quantify adhesion forces, and Young's modulus of the sample. Overall, the versatility of AFM allows a cross over to many disciplines in the science community.

## 1.7 Previous Work

AFM was used in several previous experiments and numerical models investigating van Der Waals force and adhesion. Heim *et al.* (1999) used AFM to measure the adhesion force and frictional force between silica microspheres of size 0.5 and 2.5  $\mu\text{m}$  at room temperature. Microspheres were glued using epoxy heat resin to a substrate, and to the cantilever as a tip. The force between the two was calculated by obtaining a force curve and measuring the cantilever deflection as a function of tip-sample separation. The deflection was converted to the force using the spring constant of the cantilever. Applying the JKR (Johnson, Kendall, and Roberts) and DMT (Derjaguin, Muller, and Toporov) models of cohesive force interactions to these results, they found that surface roughness decreases the adhesion force, and the DMT model more accurately matched the adhesion values.

## 1.8 Thesis structure

The remainder of this thesis describes the initial experiments that were undertaken to explore the feasibility of obtaining AFM measurements of realistic regolith simulants. In Chapter 2, we outline the methods used to acquire the data, including the samples and AFM techniques used. In Chapter 3 we discuss the initial results, including measurement and calibrated data. Finally, in Chapter 4 we discuss the implications of these results, measurement challenges, and future work.

## CHAPTER 2: METHODS

### 2.1 JSC 1- Sample

JSC-1 is a predominantly glass basaltic ash, which is similar in composition, mineralogy, and particle size distribution to lunar mare soil. JSC-1 was produced for engineering studies for human exploration on the moon, which includes the handling, excavation, and transportation of lunar soil. It has also been used to research dust dynamics, agriculture, and spacesuit durability (McKay *et al.*, 1994). JSC-1 was mined from vents caused by the Merriam crater in Flagstaff, AZ, and the ash was coarsely sieved and comminuted in an impact mill to break the material down by colliding it with other ash particles to prevent less mineral contamination. The ash was then air dried for 2 months before being placed into a plastic bag where it was heat sealed at 600° C for an hour in argon (McKay *et al.*, 1994). Figure 5 shows the approximate bulk elemental composition of JSC-1 in comparison to Apollo lunar soil. The minerals in JSC-1 have been characterized by x-ray diffraction (XRD), optical microscopy, and Scanning Electron Microscopy (SEM).

Oxide	JSC-1 (mean of 3)		Lunar Soil 14163*	
	Conc.	Std. Dev.	Conc.	
	Wt %	Wt %	Wt %	
SiO <sub>2</sub>	47.71	0.10	47.3	
TiO <sub>2</sub>	1.59	0.01	1.6	
Al <sub>2</sub> O <sub>3</sub>	15.02	0.04	17.8	
Fe <sub>2</sub> O <sub>3</sub>	3.44	0.03	0.0	
FeO	7.35	0.05	10.5	
MgO	9.01	0.09	9.6	
CaO	10.42	0.03	11.4	
Na <sub>2</sub> O	2.70	0.03	0.7	
K <sub>2</sub> O	0.82	0.02	0.6	
MnO	0.18	0.00	0.1	
Cr <sub>2</sub> O <sub>3</sub>	0.04	0.00	0.2	
P <sub>2</sub> O <sub>5</sub>	0.66	0.01	---	
LOI	0.71	0.05	---	
<b>Total</b>	<b>99.65</b>		<b>99.8</b>	

LOI = Loss on ignition \* Papike et al (1982)

Figure 5. Bulk Elemental composition of JSC-1 simulant as compared to Lunar soil. Credit: McKay *et al*, 1994

As seen in Figure 5, the three major minerals present in JSC-1 are plagioclase, pyroxene, and olivine, with minor oxides ilmenite, chromite, and clay. The plagioclase is blocky and can be several hundred micrometers in size while the pyroxene and olivine are blocky to sub-rounded and range to about 100  $\mu\text{m}$ . Ilmenite and Chromite components are less than 10  $\mu\text{m}$  in diameter and appear as swarms of rounded crystals. JSC-1 is similar in particle size distribution as sub mature lunar soil but is better sorted leading to a narrower particle size distribution than most lunar soil samples. Figure 6 shows a typical grain composition of JSC-1 simulant.

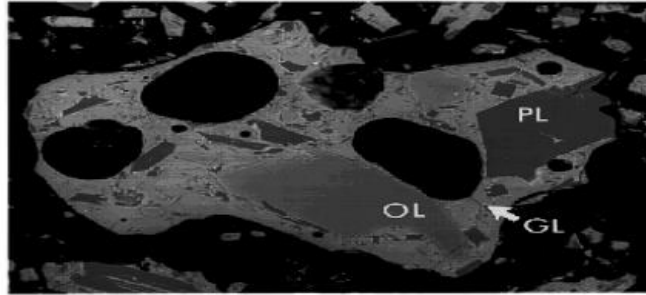


Figure 6. Cross-section of a typical JSC-1 simulant grain consisting of Glass (GL), Olivine (OL), and Plagioclase (PL). Credit: McKay *et al.*, 1994

## 2.2 AFM Operation

There are generally three modes for AFM which are contact mode, non-contact mode, and tapping mode. Contact mode is the most widely used AFM mode and the one used for this study. In contact mode, the tip exerts a constant force on the sample and as the tip scans the surface in a dragging motion. The cantilever is deflected vertically because of topographical changes. While contact mode is the most used, it can easily damage the surface and the cantilever because of the dragging, which can dislodge weakly adhered substrates and fragile samples (Taram *et al.*, 2017).

In non-contact mode, imaging takes a long-range force that exists between the tip and the sample. Non-contact mode avoids contact with the surface and relies on the attractive forces of the sample and the oscillation of the cantilever. Finally, tapping (or AC) mode, maps the topography of the surface by lightly tapping the surface with an oscillating tip. The cantilever's amplitude changes with the topography and the image is generated by monitoring the changes in amplitude. Tapping mode is generally preferred for soft matter, powders, or small particles.

### 2.2.1 Force Curves

One of the basic results of contact measurements, AFM force-distance curves constitute a fundamental tool to study surface interactions and forces. It is used in a variety of research fields including biology, biochemistry, materials engineering, and in recent years astronomy. Force-distance curves are used to study nanomechanical properties of a sample including elasticity, surface charge density, and adhesion (Capella and Dietler, 1999). In 1988, the first surface forces were measured on graphite.

Figure 7 shows an example of force curve along with a cartoon of the tip deformation at each step of acquiring the curve. At point A, the tip is approaching the sample with no (or low) interaction. At point B, the tip snaps to the surface of the sample and begins pushing down on the sample (point C), leading to a change in the curvature of the cantilever. At point D, the tip is pulling out of contact from the surface and retracting away (point E). The measurement of the difference in force from point E to the force in point A corresponds to the adhesive force between the tip and the sample, and depends on the characteristics of the tip, sample, and environment where the curves are acquired.

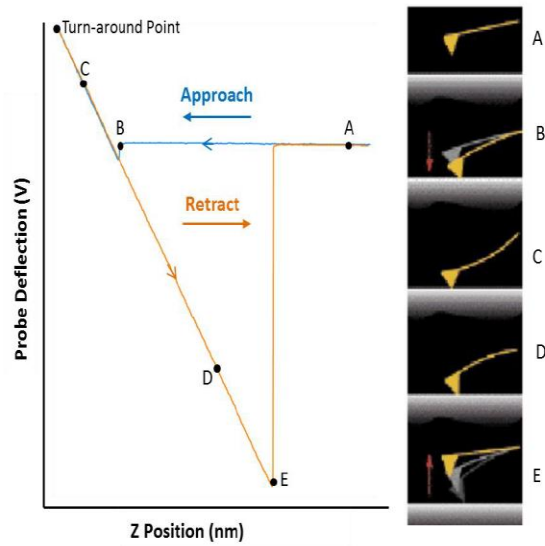


Figure 7. Example force curve showing the approach to the sample (A), the snap in of the tip to the sample (B), the local deformation of the sample (C), the initial retracting of the tip from the sample (D), and the complete removal of the tip from the sample (E)

## CHAPTER 3: RESULTS

### 3.1 Experimental Setup

Our scientific goal is to model asteroid surfaces, specifically by understanding the cohesive forces at the nanoscale that act as a glue to hold rubble piles/strengthless bodies together and influence particle motion. In order to achieve this, we employed AFM techniques to investigate the cantilever tip-sample interaction thereby allowing us to measure and quantify the adhesive force. In our experiment we used three samples, each of different grain sizes of JSC-1 simulant: a 125-250  $\mu\text{m}$  sample, a 75-125  $\mu\text{m}$  sample, and a less than 45  $\mu\text{m}$  sample. AFM cantilevers are often made of silicon, in a rectangular or “V” shape, but can be customized with coatings and with desired tips. For this study we used two tips of different shapes (pyramidal, sphere) and other characteristics, which are described in Figure 8. Each sample was attached to a silicon substrate with glue and then mounted in the AFM. On each sample we selected 2-3 grains, acquiring about 100 curves in a 3  $\mu\text{m}$  by 3  $\mu\text{m}$  region on each grain. We then screened the curves into “normal” and “abnormal” categories (see details below) and performed our analysis on the normal curves.

Specs	Spherical Tip	Spherical Tip	Gold Tip
Diameter/Length	2 $\mu\text{m}$	15 $\mu\text{m}$	14-16 $\mu\text{m}$
Material	Silicon Dioxide	Silicon Dioxide	Silicon Dioxide
Coating	None	None	Au (Gold) – Top and Bottom
Shape	Spherical	Spherical	Pyramidal
Force Constant	1.2 N/m	2.0 N/m	0.29 N/m

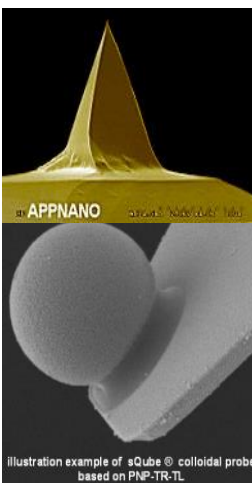


Figure 8. Picture of the characteristics of the two tips used in the experiment (right) and a table of their key characteristics, which may influence the measurements (left).

### 3.2 Force Curves Measurements

Our results include force curves from the three JSC-1 size samples. Our first series of measurements was performed using the pyramid shaped tip. Next the measurements will use spherical tips with two different diameters, 2  $\mu\text{m}$  and 15  $\mu\text{m}$ . On each sample two to three grains (rocks) were selected randomly and used to acquire force curves. On each rock, the area probed was 3  $\mu\text{m}$  by 3  $\mu\text{m}$  area in which 100 curves were obtained for each grain (rock). Our results present typical force curves similar to those shown in section 2.2.1, while other measurements produced complex force curves. We separated the curves into two categories of “normal” and “abnormal” curves and conducted all our analyses on the normal curves across all samples and tips. Figures 9, 10, and 11 show the normal force curves on each tip for less than 45  $\mu\text{m}$  sample.

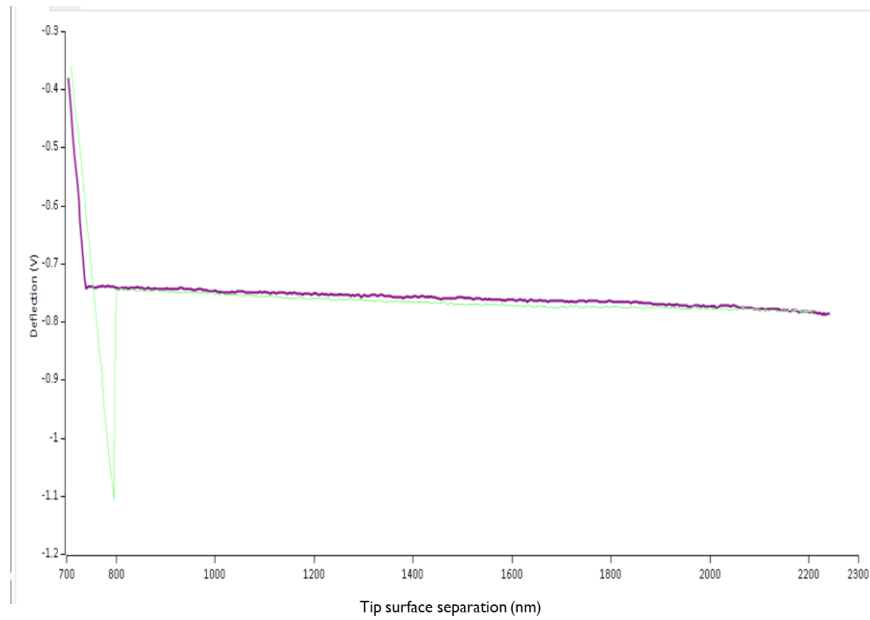


Figure 9. A force-separation curve of the pyramid shaped tip on the less than 45  $\mu\text{m}$  sample, showing the deflection in volts (V) and the displacement in nm.

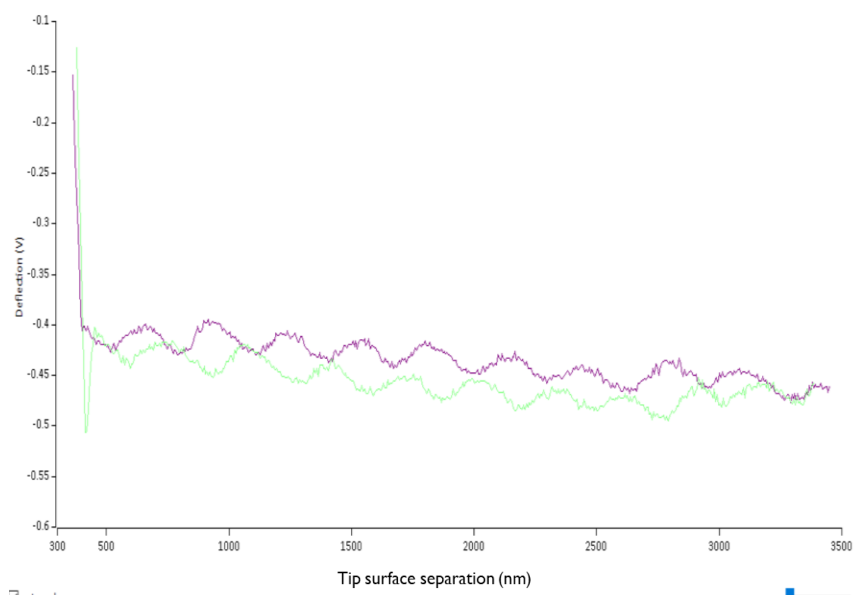


Figure 10. A force-separation curve of the 2  $\mu\text{m}$  sphere on the less than 45  $\mu\text{m}$  sample. Oscillations in the approach and retract curves are attributed to the limitations of the system.

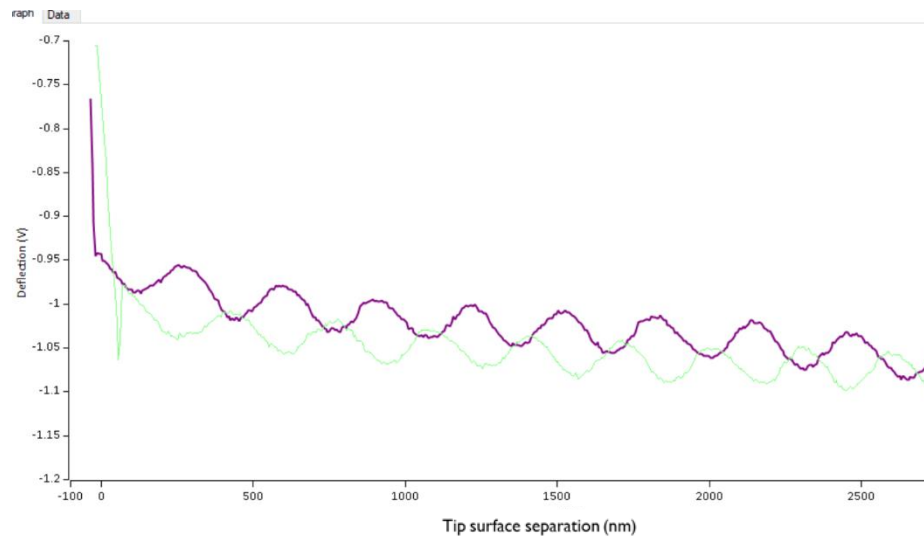


Figure 11. the force displacement curve of the 15  $\mu\text{m}$  sphere on the 125-250  $\mu\text{m}$  sample. Oscillations in the approach and retract curves are attributed to the machine and the cantilever

### 3.2.1 Abnormal Curves

Some of the force curves measured in our experiment were classified as “abnormal” curves that were difficult to understand and thus extract adhesive values. These curves consist of oscillations from the machine (also seen in the normal curves) and complex dips in the force curve measurements, which we discuss in Chapter 4. The figures below are examples of abnormal curves from each tip on the 75-125  $\mu\text{m}$  JSC-1 sample.

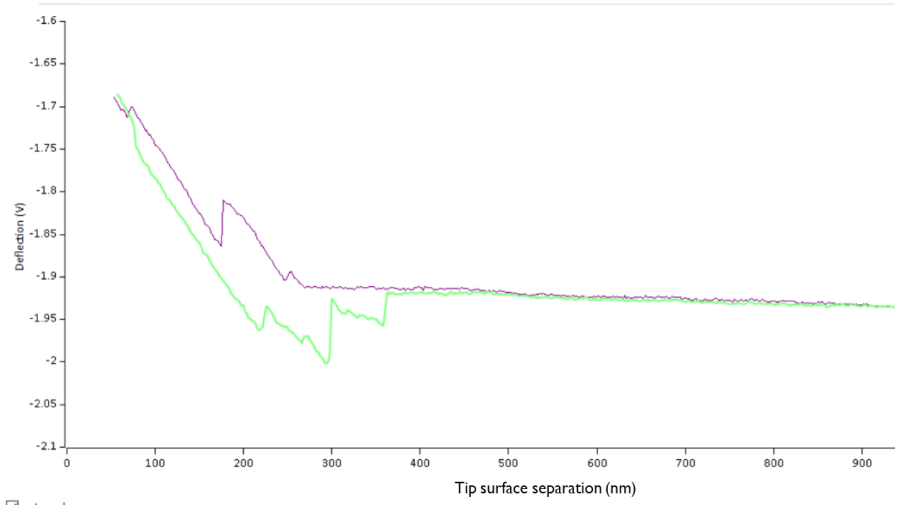


Figure 12. An example of abnormal force curve obtained on the 75-125  $\mu\text{m}$  sample using the pyramid gold tip.

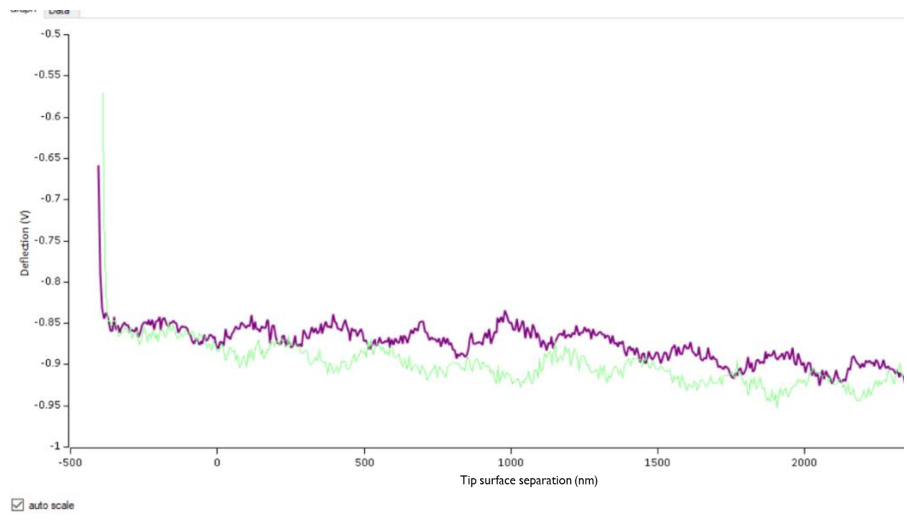


Figure 13. An example of abnormal force curve obtained with the 2  $\mu\text{m}$  sphere, on the 75-125  $\mu\text{m}$  sample.

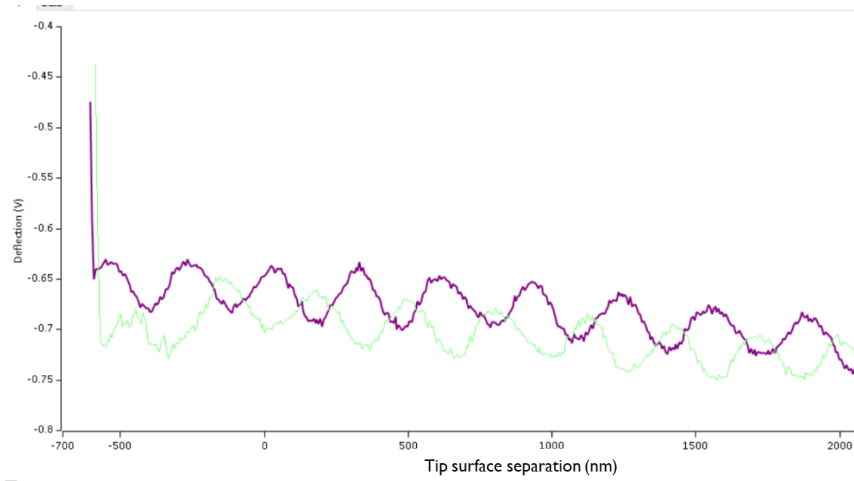


Figure 14. An example of abnormal curve obtained from the 15  $\mu\text{m}$  sphere tip on the < 45  $\mu\text{m}$  sample.

### 3.3 Calibration

To extract the force values of the curves, we converted the deflection to force. In order to convert the deflection, we used a method described by Ohler (2007), which models the cantilever as a simple harmonic oscillator. The thermal motion of the cantilever's oscillation is related to its thermal energy by the equation

$$k = \frac{K_B T}{\langle z_c^2 \rangle} \quad (3)$$

where  $K_B$  is the Boltzmann constant,  $T$  is the temperature, and  $\langle z_c^2 \rangle$  is the mean square displacement of the cantilever. The means square displacement can be found by thermally tuning the cantilever and acquiring the  $V_{\text{rms}}$  value. After tuning, we calibrated the tip by taking a set of 13 force curves on a hard surface, like glass, averaging the slopes of all the curves, and dividing the  $V_{\text{rms}}$  by the average slope to find  $\langle z \rangle$ . Following that, we multiplied the result by  $10^{-9}$  to present the value in nm and used Equation 3 to acquire the cantilever spring constant.

### 3.4 Histograms

In order to assess the variability in our datasets, we compiled our results of force measurements into histograms that allow us to see the distribution of force values across the samples. The adhesion values for the pyramid-shaped tip force values were obtained through the Analysis Studio program (Anasys Instrument). The “snap-in” function is an automated system configuration that fits a force curve and measures the adhesion force by calculating the value from the baseline to the lowest part of the curve, which is noted as the point of maximum adhesion. To convert the snap-in values, given in V/nm, we divided them by the average slope and multiplied the result by the previously calculated spring constant, given in nN/nm, to acquire a force unit of nN. The figures below show the comparison of each sample probed with the gold pyramid-shaped tip on 2-3 different grains (rocks) per sample.

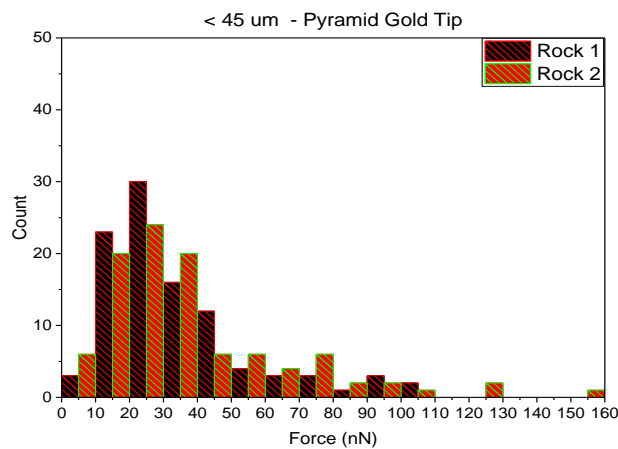


Figure 15. Histogram displaying the distribution of measured adhesion force values between 2 grains on the < 45 μm sample and the pyramid-shaped tip.

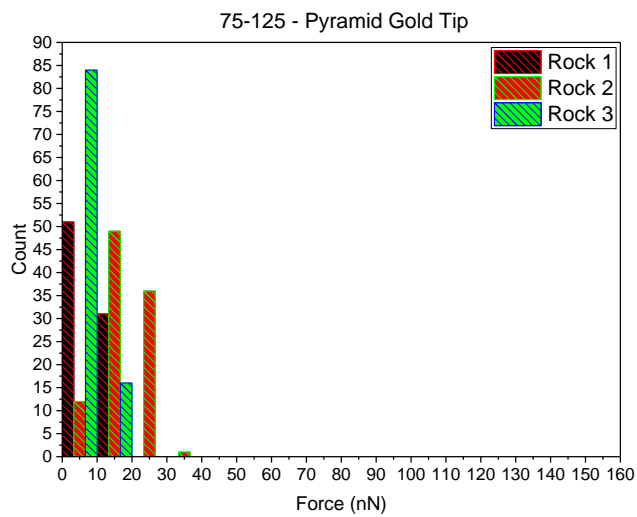


Figure 15. Histogram displaying the distribution of measured adhesion force values between 3 grains on the 75-125  $\mu\text{m}$  sample and the pyramid-shaped tip.

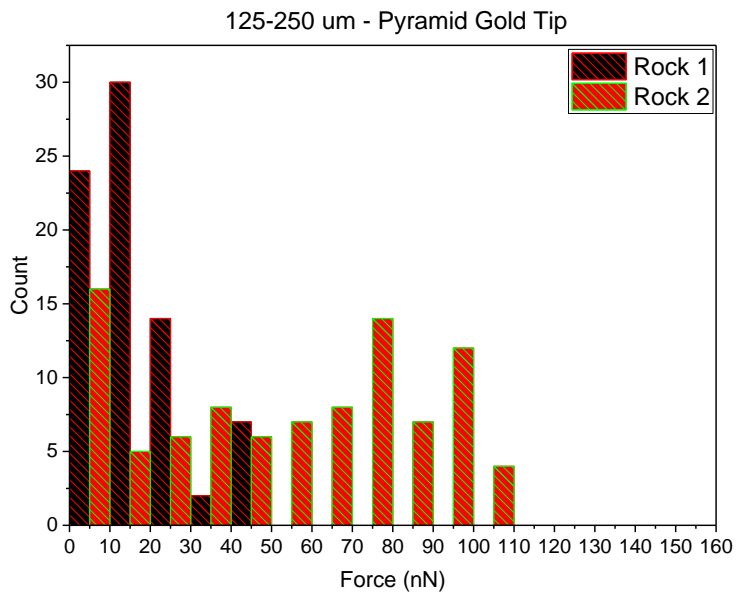


Figure 16 Histogram displaying the distribution of measured adhesion force values between 2 grains on the 125-250  $\mu\text{m}$  sample and the pyramid-shaped tip.

### 3.4.1 2 $\mu\text{m}$ Spherical Tip Histograms

In the second part of our analysis, we analyze the spherical tips measurements using a Python code that reads in the data file, determines the size of the data, averages the baseline of the curve, and subtracts the baseline value of each curve from the deflection value (in volts) of the retract curve. We then convert the values into the adhesion force (nN). The results below show histograms of the 2  $\mu\text{m}$  and 15  $\mu\text{m}$  sphere across the samples on 2-3 grains (rocks) on each.

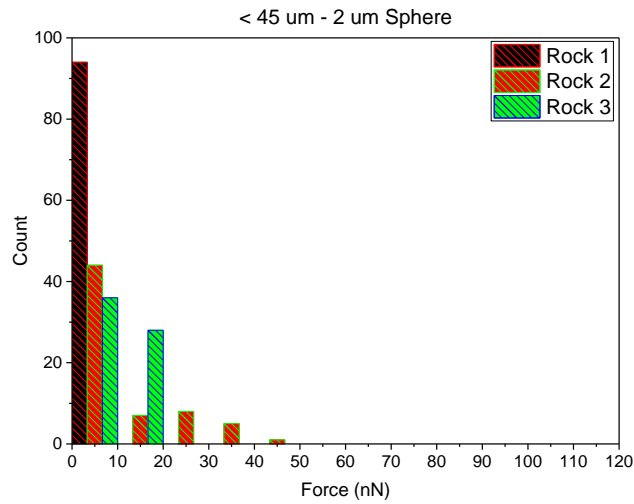


Figure 17 Histogram displaying the distribution of measured adhesion force values between 3 grains on the < 45  $\mu\text{m}$  sample and the 2  $\mu\text{m}$  spherical tip.

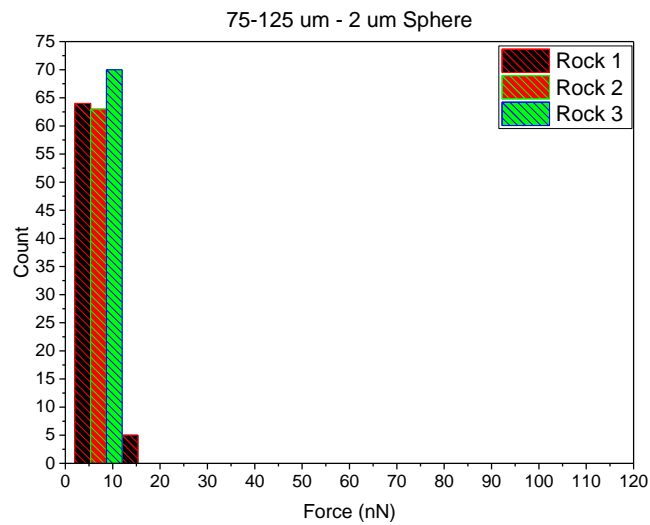


Figure 18. Histogram displaying the distribution of measured adhesion force values between 3 grains on the 75-125 μm sample and the 2 μm spherical tip

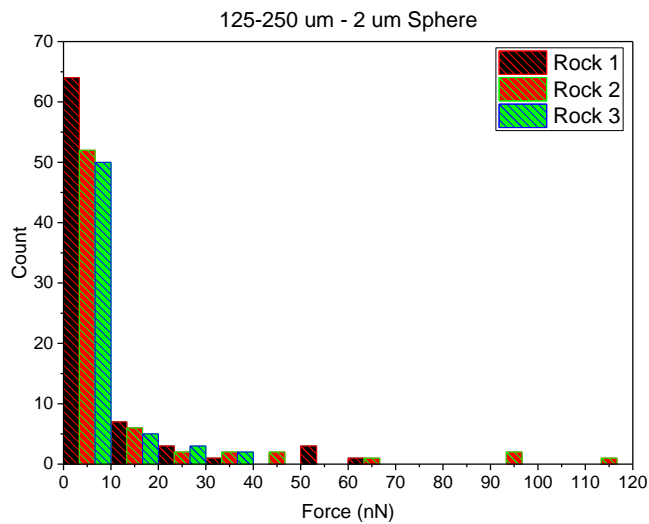


Figure 19 Histogram displaying the distribution of measured adhesion force values between 3 grains on the 125-250 μm sample and the 2 μm spherical tip.

### 3.4.2 15 $\mu\text{m}$ Histograms

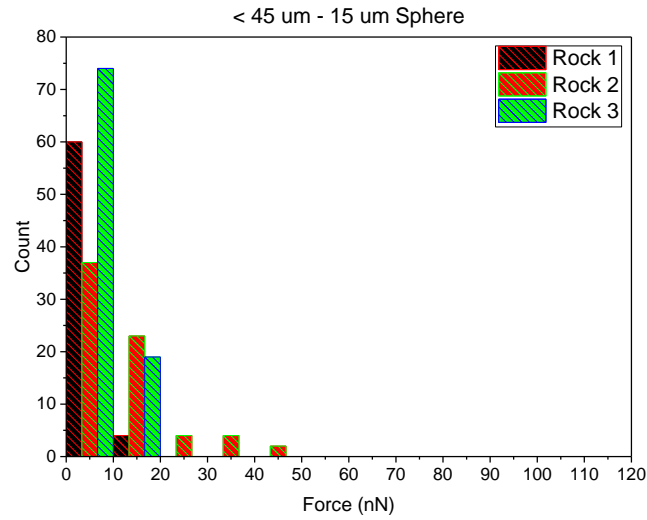


Figure 20. Histogram displaying the distribution of measured adhesion force values between 3 grains on the < 45  $\mu\text{m}$  sample and the 15  $\mu\text{m}$  spherical tip

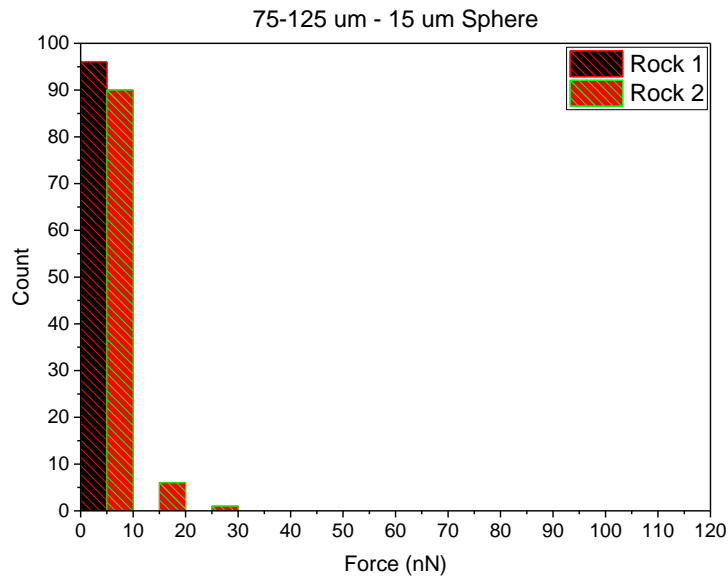


Figure 21. Histogram displaying the distribution of measured adhesion force values between 2 grains on the 75-125  $\mu\text{m}$  sample and the 15  $\mu\text{m}$  spherical tip

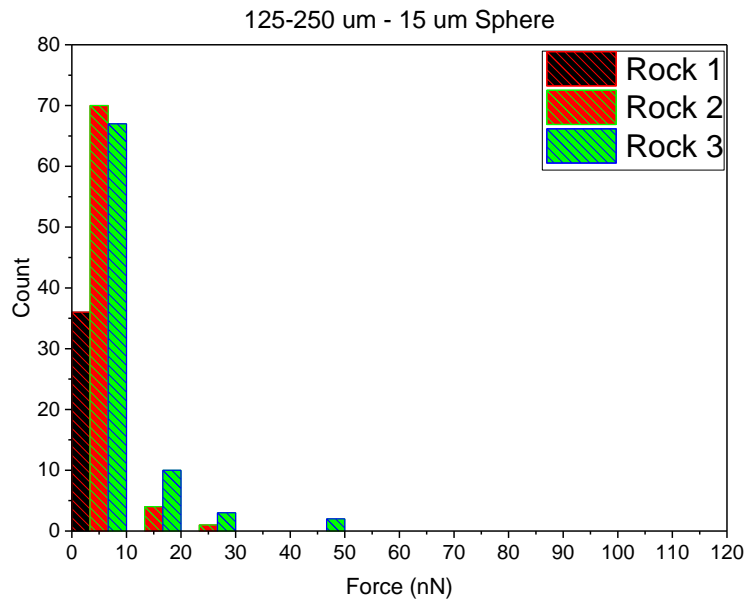


Figure 22. Histogram displaying the distribution of measured adhesion force values between 3 grains on the 125-250  $\mu\text{m}$  sample and the 15  $\mu\text{m}$  spherical tip.

### 3.5 Comparison of Histograms

Comparing the histograms of the adhesion forces measured by the three tips allows us to compare the distribution of adhesion force values and how they vary based on sample and tip as shown below in Figure 20. We see similar results between the results of the two spherical tips, but the pyramidal tip show significantly higher and a wider range of adhesion values.

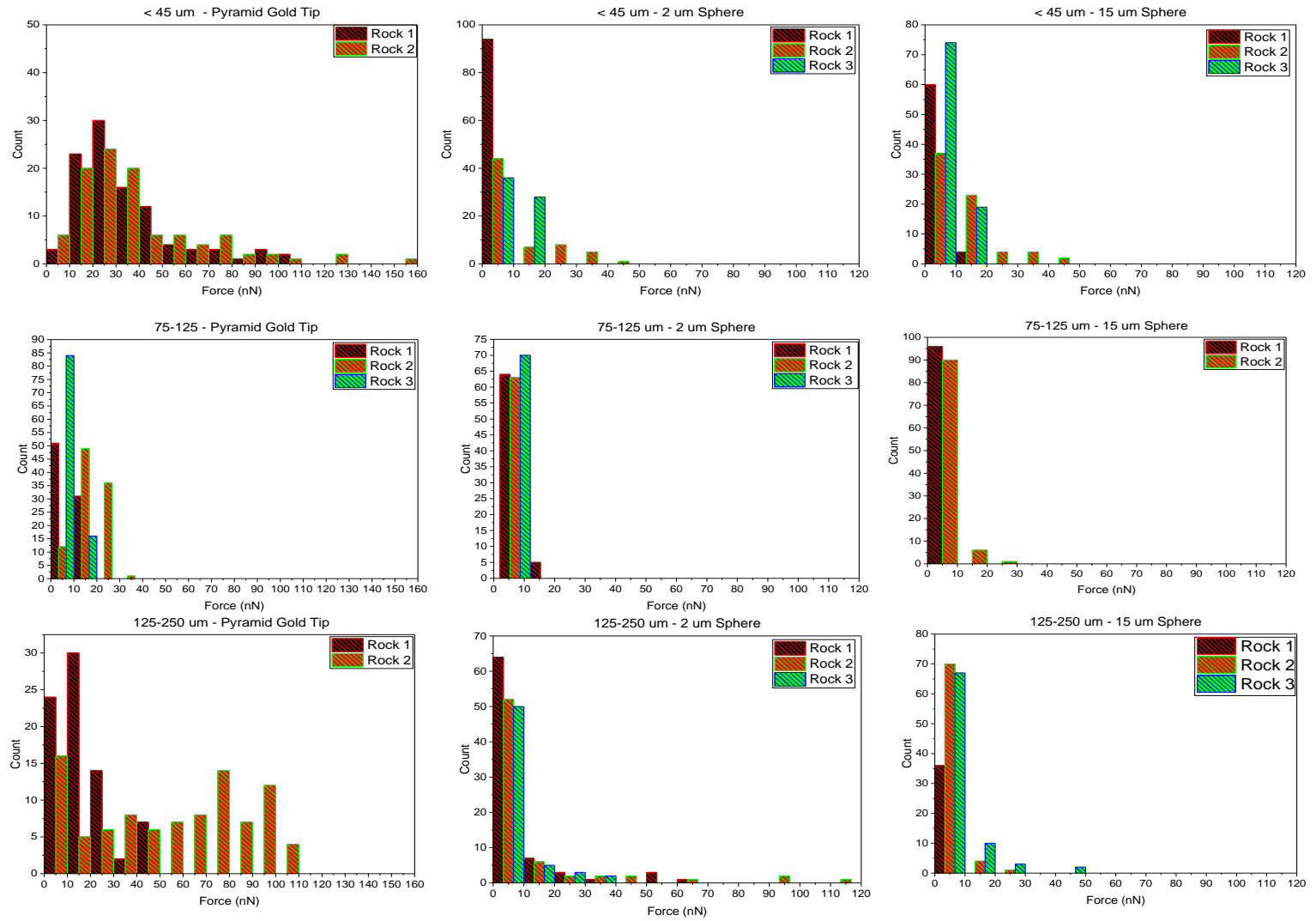


Figure 23. Pyramid-shaped tip vs. 2 $\mu$ m spherical tip vs 15  $\mu$ m spherical tip. Comparison of histograms across all samples and tip types.

## CHAPTER 4: DISCUSSION

### 4.1 Interpretation of the Results

Based on previous work, we expected that we would measure larger adhesion forces with the spherical tips than the pyramidal tip. The larger surface area of the spheres should create a larger contact area of the sphere to the sample, which should lead to higher forces. Our results, however, appear to show that the adhesion values for the pyramidal tip produced larger forces and a longer-range distribution of those forces. These results must be taken in context, however, and we explore the other factors that may have influenced these measurements.

A study by Capella and Dietler (1999) revealed that when acquiring force curves in air, ambient humidity in the room impacted the measurements by creating a meniscus from the thin water layer, which influenced the forces felt as the tip interacted with the surface. This capillary force can shadow the effect of other interactions between the sample and the tip. While the humidity levels were similar on different days of measurements, it is possible that humidity affected the measured contact forces of the sphere and pyramid-shaped tips. By controlling the environment, we expect to gain a better understanding of the extent of this interference with our measurement

It is also key to identify the properties of the selected tips that will influence these measurements. The coating on the tips of the cantilever can contribute to the resultant adhesive values. The pyramidal tip was coated throughout with Au (Gold) although it was made of silicon. The contribution of gold to adhesion was not explored in our experiment but it can affect the adhesion of the tip to the sample because it is a conductor and has very different electrical

properties. The spherical tips were not coated but were made of silicone dioxide ( $\text{SiO}_2$ ), which will impact the adhesive and cohesive properties measured between the sample based on the composition of the JSC-1 simulant and the grains themselves. The stiffness, or k value, of the cantilevers can also influence the contact region of the tip and the sample which can affect the applied force on the contact area. As we investigate further, we will consider these effects, their relationships and how they factored into adhesive values.

Finally, the complicated structure of the abnormal curves made it difficult to extract adhesive values from those curves. We note that there are dips in the curves (as in Figure 12) which we infer occurred due to the tip of the cantilever adhering to smaller particles that were also present on the on the surface of the rock. SEM images shown below show the sample rock sizes and the smaller particles found on the surface of these rocks.

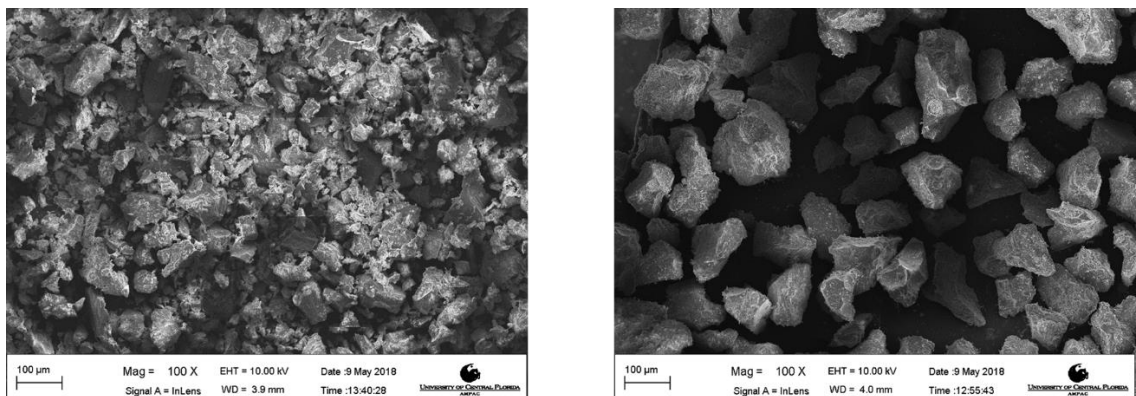


Figure 24. SEM images of the  $< 45 \mu\text{m}$  sample (left) and the  $75\text{-}125 \mu\text{m}$  sample (right). A scale is shown in the bottom left of the picture for size comparisons.

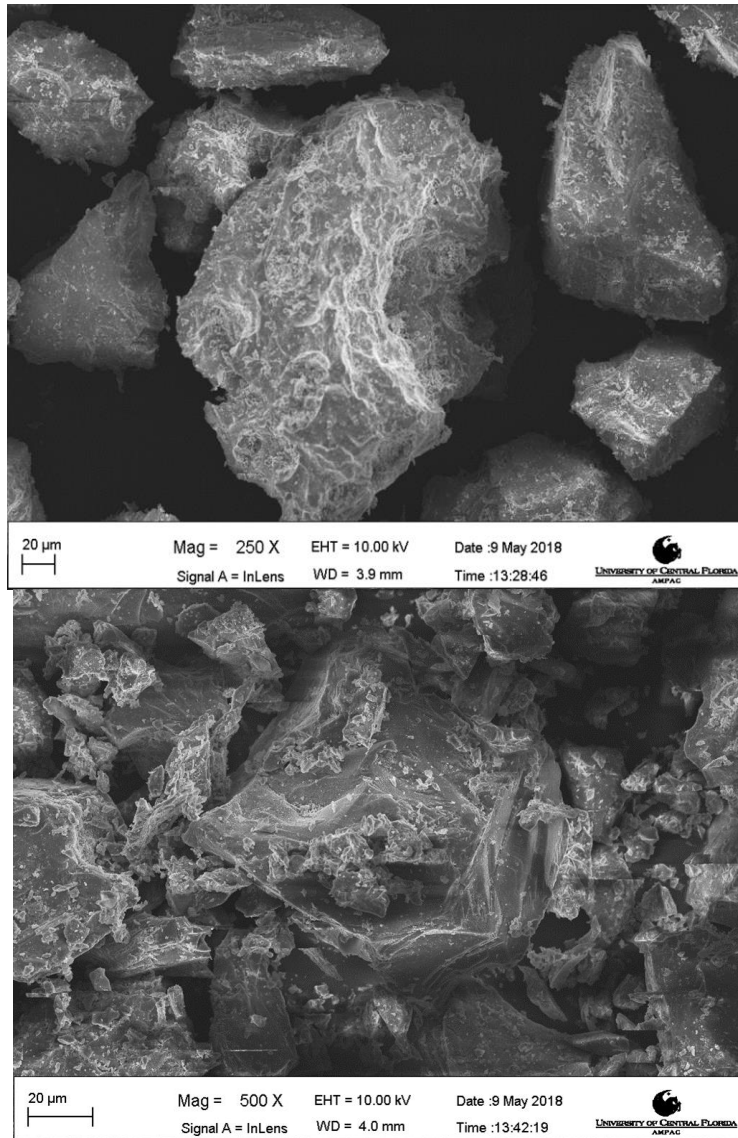


Figure 25 Top: SEM image of the 75-125 µm sample magnified to 250 X displaying smaller particles on the surface of a rock. Bottom: SEM image of the 75- 125 µm sample magnified to 500 X displaying the smaller particles littering the surface of a rock.

## 4.2 Future Work

To further our investigation, we intend to extract the Young's Modulus and the energy dissipated from the force curves as shown in Figure 26. Analyzing the abnormal curves can also provide us with insight into the nature of the interactions that take place between the measurement tip and the grains when smaller particles are present on the main grains of interest. To understand contact mechanics in more detail, we can perform sphere-to-sphere interactions and compare the results to enhance our knowledge and provide another basis of comparison for our further experiments. Varying the humidity in the chamber can also lead us to more conclusive evidence of how humidity affects the adhesion of the tip and sample. Extending from that, performing these experiments in vacuum would more accurately simulate the space environment, and would greatly reduce these additional surface contamination effects. Finally, the ultimate goal is to perform experiments of rock-to-rock interactions by attaching a grain to the cantilever and using that as the "tip" to acquire force curves between that and the grains in the simulant.

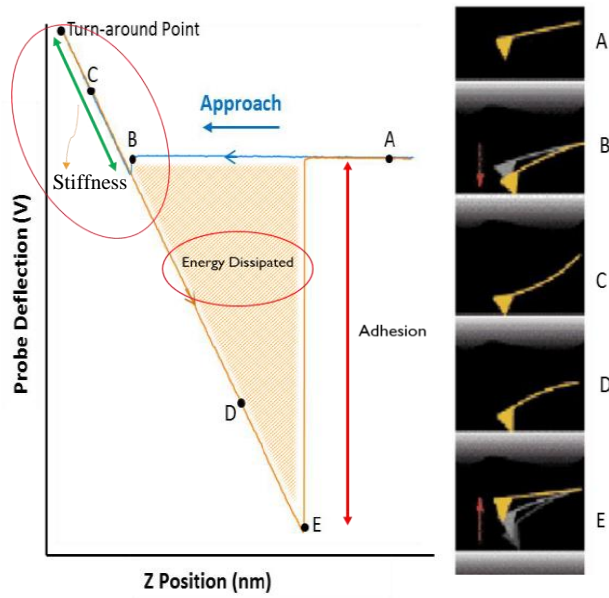


Figure 26. Generic force curve showing the properties of the material and cantilever you can extract from a force curve. The circled properties are priorities for future analysis.

## REFERENCES

- Asphaug E, Ryan E, Zuber M. 2002. Asteroid interiors. In *Asteroids III* (W. F. Bottke Jr. et al., eds.), this volume. Univ. of Arizona, Tucson
- Binning G, Quate CF, Gerber C: Atomic force microscope, *Phys Rev Lett* 56(9):930–933, 1986.
- Bottke WF, Durda DD, Nesvorný D, Jedicke R, Morbidelli A, et al. 2005. The fossilized size distribution of the main asteroid belt. *Icarus* 175(1):111–40
- Britt, D.T., Yeomans, D., & Consolmagno, G.J. (2002). Asteroid Density, Porosity, and Structure.
- Cappella, B., & Dietler, G. (1999). Force-distance curves by atomic force microscopy. *Surface Science Reports*, 34(1-3), 1-104. doi:10.1016/s0167-5729(99)00003-5
- Chapman CR. 1978. Asteroid collisions, craters, regolith, and lifetimes. In *Asteroids: An Exploration Assessment*, ed. D. Morrison and W. C. Wells, pp. 145–160. NASA Conf. Publ. 2053.
- Dombard, A. J., Barnouin, O. S., Prockter, L. M., & Thomas, P. C. (2010). Boulders and ponds on the Asteroid 433 Eros. *Icarus*, 210(2), 713-721. doi:10.1016/j.icarus.2010.07.006
- Fujiwara A, Kawaguchi J, Yeomans DK, Abe M, et al. 2006. The Rubble-Pile Asteroid Itokawa as Observed by Hayabusa. *Science* 312:1330-1334
- Giessibl FJ: Advances in atomic force microscopy, *Rev Mod Phys* 75(3):949–983, 2003.
- Gomes S, Trannoy N, Grossel P, Depasse F, Bainier C, Charrat D: DC scanning thermal microscopy: characterisation and interpretation of the measurement, *Int J Thermal Sci* 40(11):949–958, 2001.

- Gundlach B, Blum J. 2013. A new method to determine the grain size of planetary regolith. *Icarus* 223:479-492
- Hartzell, Christine M., "The Dynamics of Near-Surface Dust on Airless Bodies" (2012). *Aerospace Engineering Sciences Graduate Theses & Dissertations*. 48. [https://scholar.colorado.edu/asen\\_gradetds/48](https://scholar.colorado.edu/asen_gradetds/48)
- Heim, L., Blum, J., Preuss, M., & Butt, H. (1999). Adhesion and Friction Forces between Spherical Micrometer-Sized Particles. *Physical Review Letters*, 83(16), 3328-3331. doi:10.1103/physrevlett.83.3328
- Holsapple KA. 1994. Catastrophic disruptions and cratering of Solar System bodies: A review and new results. *Planetary and Space Science* 42(12):1067-1078
- Housen, K. R., & Holsapple, K. A. (2011). Ejecta from impact craters. *Icarus*, 211(1), 856-875. doi:10.1016/j.icarus.2010.09.017
- Jalili N, Laxminarayana K: A review of atomic force microscopy imaging systems: application to molecular metrology and biological sciences, *Mechatronics* 14(8):907–945, 2004.
- Jeffreys, H. (1947). The Effects of Collisions on Saturns Rings. *Monthly Notices of the Royal Astronomical Society*, 107(3), 263-267. doi:10.1093/mnras/107.3.263
- Kiuchi, M., & Nakamura, A. M. (2014). Relationship between regolith particle size and porosity on small bodies. *Icarus*, 239, 291-293. doi:10.1016/j.icarus.2014.05.029
- Matsumura, S., Richardson, D. C., Michel, P., Schwartz, S. R., & Ballouz, R. (2014). The Brazil nut effect and its application to asteroids. *Monthly Notices of the Royal Astronomical Society*, 443(4), 3368-3380. doi:10.1093/mnras/stu1388
- Ohler, Ben. (2007). Practical Advice on the Determination of Cantilever Spring Constants. Inc. Internal Publ.

- Öpik EJ. 1966. Sun-grazing comets and tidal disruption. *Irish Astron. J.* 7:141–161
- Richardson DC, Leinhardt ZM, Melosh HJ, Bottke WF Jr, Asphaug E. 2002. Gravitational aggregates: evidence and evolution. See Bottke et al. 2002a, pp. 501–15
- Roche EA. 1847. *Acad. Sci. Lett. Montpelier. Mem. Section Sci.* 1:243
- Sanchez P and Scheeres D.J. 2014. “The Strength of Regolith and Rubble Pile Asteroids,” *Meteoritics and Planetary Science*, 49(5): 788-811
- Scheeres D.J, Hartzell C.M, Sanchez P, Swift M, “Scaling forces to asteroid surfaces: The role of cohesion”, *Icarus*, Volume, 210, Issue 2, 2010, Pages 968-984
- Scheeres, D. S., Britt, D., Carry, B., & Holsapple, K. A. (2015). Asteroid Interiors and Morphology. *Asteroids IV*. doi:10.2458/azu\_uapress\_9780816532131-ch038
- Stadelmann T: Review of scanning probe microscopy techniques, 2016, disponível em: <<http://timstadelmann.de/spmreview.pdf>>
- S. McKay, David & L. Carter, James & Boles, Walter & C. Allen, Carlton & H. Allton, Judith. (1993). JSC-1: A new lunar regolith simulant. *Lunar Planet. Sci.* 24. 963-964.
- Tararam, R., Garcia, P. S., Deda, D. K., Varela, J. A., & Leite, F. D. (2017). Atomic Force Microscopy: A Powerful Tool for Electrical Characterization. *Nanocharacterization Techniques*, 37-64. doi:10.1016/b978-0-323-49778-7.00002-3
- Veverka, J., et al. (2000), Near at Eros: Imaging and spectral results, *Science*, 289, 2088–2097, doi:10.1126/science.289.5487.2088.
- Walsh, K. J. (2018). Rubble Pile Asteroids. *Annual Review of Astronomy and Astrophysics*, 56(1), 593-624. doi:10.1146/annurev-astro-081817-052013